Single-mode surface-emitting distributed feedback quantum-cascade lasers based on hybrid waveguide structure

Wanhong Guo (郭万红), Junqi Liu (刘俊岐)*, Jianyan Chen (陈剑燕), Lu Li (李 路), Lijun Wang (王利军), Fengqi Liu (刘峰奇), and Zhanguo Wang (王占国)

Key Laboratory of Semiconductor Materials Science, Institute of Semiconductors, Chinese Academy of Sciences, Beijing 100083, China

**Corresponding author: jqliu@semi.ac.cn*

Received December 2, 2010; accepted January 20, 2011; posted online April 28, 2011

Surface-emitting distributed feedback quantum-cascade lasers operating at $\lambda \approx 7.8$ μm are demonstrated. The metal-covered second-order grating is shallow-etched into the surface of a thin InGaAs contact and cladding layer. This forms a hybrid waveguide and used to achieve relatively low waveguide losses and high coupling strengths. The devices exhibit stable single-mode operation from 90 to 130 K with a side mode suppression ratio above 20 dB. A slope efficiency of 194 mW/A is obtained at 90 K, which is twice higher than that of the Fabry-Perot counterpart.

OCIS codes: 140.5965, 230.1950, 250.7270, 250.7360.
doi: 10.3788/COL201109.061404.

Since the first demonstration of quantum-cascade lasers (QCLs) in 1994, the steady improvement allowed this kind of lasers to become compact and powerful semiconductor light sources in mid- and far-infrared spectral regions[1−3]. For numerous practical applications, such as chemical sensing and pollution monitoring, QCLs with single-mode operation and surface emission with low beam divergence are highly desirable because these facilitate high-sensitivity detection and two-dimensional (2D) integration. Due to the polarization selection of intersubband transition, QCLs cannot be fabricated directly into vertical-cavity surface-emitting structure[4] as generally done in interband semiconductor lasers. Second-order distributed feedback (DFB) gratings capable of surface emission via their first-order Fourier diffraction have been widely used in QCLs because of their well-developed theories and experimental demonstrations. To date, most of previously reported second-order gratings have been etched into standard dielectric waveguides, where the deep-etched grating with a high aspect ratio is required to obtain sufficient refractive index contrast and coupling coefficient[5−11]. On the other hand, gratings solely patterned in the metal contact for surface plasmon waveguide QCLs will result in large values for both refractive index contrast and coupling coefficient. However, high waveguide losses induced by the highly lossy surface plasmon limit the device performance, affecting the possibility for further improvements[12].

We propose and demonstrate surface-emitting DFB QCLs based on a hybrid waveguide design–an intermediate structure between standard dielectric waveguide and surface-plasmon waveguide, where a thin InGaAs contact and cladding layer is used instead of traditionally thick InP cladding layers. By optimizing the duty cycle of a shallow-etched second-order grating, this design can achieve relatively low waveguide losses and high coupling strengths. The resulting devices exhibit stable single-mode operation with a side mode suppression ratio (SMSR) above 20 dB.

The core of our waveguide design consists of a 2.45-μm-thick active region (Si, average doping $\sim 4\times10^{16}$ cm^{-3})[13] sandwiched between a top 0.5-μm-thick $In_{0.52}Ga_{0.48}As$ layer (Si, 4×10^{16} cm^{-3}) and a bottom 0.4-μm-thick $In_{0.52}Ga_{0.48}As$ layer (Si, 4×10^{16} cm^{-3}). The cladding layers are composed of a 0.4-μm-thick high-doped $In_{0.52}Ga_{0.48}As$ contact (Si, 2×10^{18} cm^{-3}) on top and a low-doped InP substrate (Si, 3×10^{17} cm^{-3}) at the bottom. Based on this waveguide structure, a second-order grating in 0.4-μm deep is etched into the top high-doped InGaAs contact layer. Thus, the absorption losses induced by this high-doped layer are minimized in the grating trough. For a clear result, simulation was carried out with the method presented in Ref. [14]. Figure 1(a) shows the calculated coupling coefficient and waveguide loss as a function of the grating duty cycle. For small duty cycles, the coupling coefficient is small because of the weak perturbation of refractive index. The waveguide loss is low because of small absorption loss. For large duty cycles, the coupling coefficient becomes large due to the high overlap between the optical field and the grating caused by the rise of average refractive index in the grating region. On the other hand, the waveguide loss increases due to the surface plasmon pinning at the metal-semiconductor interface. Weighing the trade-off between the coupling coefficient and waveguide loss, the duty cycle was determined to be 0.6, where a relatively low waveguide loss of 18 cm^{-1} and a relatively high coupling coefficient κ of 48.3+13.8i were achieved. Following this grating design, we calculated transverse mode profiles of waveguide structures in the grating trough and in the grating peak, shown in Fig. 1(b). The profile mismatch between these two modes is significant, since the surface-plasmon waveguide in the grating peak tends to bind the optical field, while the air-confinement waveguide in the grating trough repels it into the active region. This significant mismatch yields

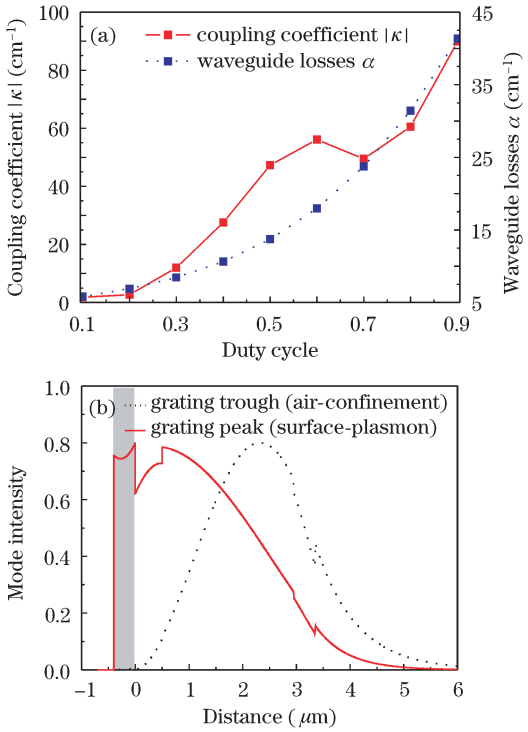

Fig. 1. (a) Calculated coupling strength and waveguide losses versus duty cycle for a 400-nm-deep grating; (b) transverse mode profiles of waveguide structures in the grating trough and in the grating peak, and the gray area corresponds to the second-order grating.

the above-calculated large coupling coefficient. Consequently, the advantage of this device structure is the achievement of relatively large coupling strength and low waveguide losses combined with simplified device preparation process, since there is no need for InP capping epitaxial growth or deep semiconductor etching.

After the material was grown by solid-source molecular-beam epitaxy, the device fabrication started with the definition of Ti/Au (10/250 nm) second-order Bragg grating with a period of Λ=2.5 μm via contact lithography and wet chemical etching. By adjusting the time of exposure and development, the expected duty cycle of σ=0.6 was realized. Subsequently, the grating was etched 0.4-μm deep into the bottom high-doped $In_{0.52}Ga_{0.48}As$ by reactive ion etching. Subsequently, 70-μm-wide and 3.5-μm-deep ridge waveguides were defined using conventional photolithography and nonselective wet chemical etching. A 250-nm-thick SiO_2 layer was subsequently deposited around the ridges for electrical insulation and 60-μm-wide windows were opened on the ridges for current injection. The Ti/Au (20/500 nm) was deposited as the top contact metal by electron beam evaporation and standard lift-off processing, and a thick Au layer of 2−3 μm was electroplated on the top contact to effectively spread the current. To allow for surface emission, the top contact metal covered only the edges of the ridge, leaving a 40-μm-wide surface emission window. Figures 2 (a) and (b) show the top and cross-sectional views of the grating. Then, the wafer was lapped down to about 150 μm and polished for back AuGeNi/Au (200 nm total) contact deposition. Finally, 1.5-mm-long laser bars were cleaved from the wafer and indium soldered to copper heat sinks with the episide up.

For device characterization, lasers were mounted on a temperature-controlled cold finger in a nitrogen flow cryostat. A repetition rate of 5 kHz and a pulse width of 2 μs were used for all temperatures. Figure 3 shows the output power-current ($L-I$) characteristics for surface-emitting DFB QCLs at temperatures between 90 and 130 K, measured using calibrated thermopiles. At 90 K, a relatively low threshold current of 2.55 A (threshold current density of 2.43 kA/cm^2) and a maximum output power of 166 mW are observed. The slope efficiency at this temperature was deduced from experimental data, that is, dP/dI=194 mW/A, which is twice higher than that of the Fabry–Perot counterpart at 80 K. This confirmed the strong coupling between the optical field and the grating structure we designed. At 130 K, 50-mW optical output power with a slope efficiency of 34 mW/A is still obtained. However, the corresponding threshold current only increased to 3.05 A (threshold current density of 2.90 kA/cm^2). By fitting the temperature dependence of threshold current density with an exponential function $J_{\rm th}=J_0\exp(T/T_0)$, a characteristic temperature of T_0=217 K is obtained.

The lasing spectra were obtained with a Fourier transform infrared (FTIR) spectrometer with a spectral resolution of 0.5 cm^{-1}. Single-mode surface emission is observed with SMSR above 20 dB for the entire working temperature range, as shown in Fig. 4. The full-width at half-maximum (FWHM) of the lasing spectra is about 0.5 cm^{-1}, which is limited by the resolution of the FTIR spectrometer in our measurement setup. The lasing spectra obtained at different heat sink temperatures between 90 and 130 K reveal a linear temperature tuning of the emission wavelength from 7.856 to 7.887 μm with a tuning coefficient of approximately 0.78 nm/K.

The far-field distribution was measured with a liquid nitrogen-cooled HgCdTe detector located 10 cm away from the rotation stage without any focusing element. Figure 5 depicts the measured beam divergence for surface-emitting DFB QCLs in two orthogonal directions. The far field along the waveguide shows an asymmetrical double-lobe pattern with a separation of 1.5°. This

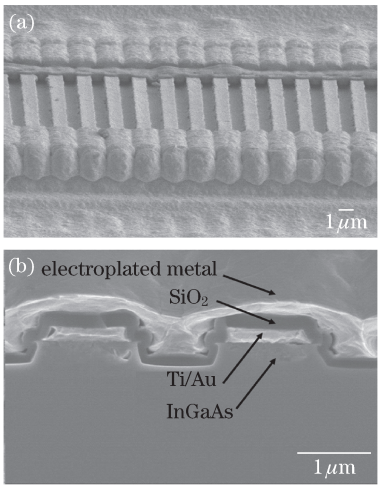

Fig. 2. Scanning electron microscopy (SEM) pictures of surface-emitting DFB QCLs. (a) Top view of the grating; (b) cross-sectional view of the device.

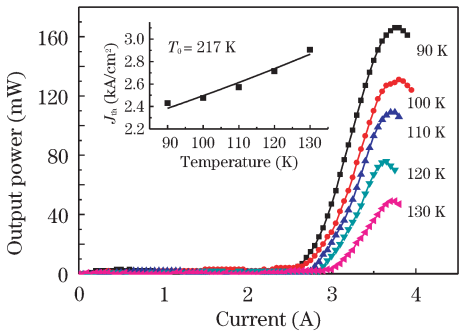

Fig. 3. *L-I* characteristics of surface-emitting DFB QCLs for different heat sink temperatures between 90 and 130 K; inset illustrates threshold current density as a function of the heat sink temperature.

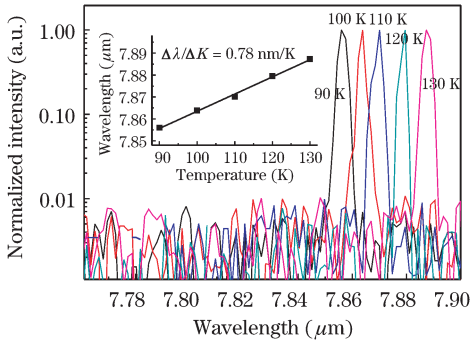

Fig. 4. Lasing spectra of the surface emitting DFB QCL for different heat sink temperatures between 90 and 130 K; inset shows the corresponding temperature dependence of the lasing wavelength where the solid line denotes a linear fit of the experimental data.

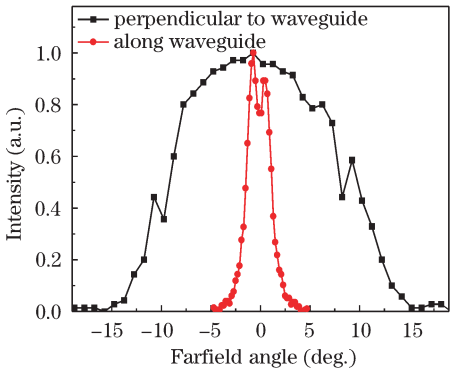

Fig. 5. Far field distributions of surface-emitting DFB QCLs in the directions along and perpendicular to the waveguide; heat sink temperature is 90 K.

double-lobe far field can be explained by the fact that the near field has the phase difference of 180° at both ends of the device, and thus the far field has a center node[15]. The asymmetry in the height of the two lobes is attributed to the arbitrary position of the end mirrors in relation to the grating. The far field perpendicular to the waveguide has an FWHM of 17°.

In conclusion, we report 7.8-μm surface-emitting DFB QCLs based on a hybrid waveguide, where a metal-covered second-order grating is shallow-etched into the surface of the waveguide. By optimizing the duty cycle of the grating, relatively low waveguide losses and high coupling strengths are obtained. Based on a coupling mechanism between surface-plasmon and air-guided modes, the devices exhibit stable single-mode operation with a side mode suppression ratio above 20 dB and a high slope efficiency of 194 mW/A at 90 K. In addition, a double-lobe far-field pattern with a separation of 1.5° is observed in the direction along the waveguide. Further work will focus on key issues, such as increasing working temperature and decreasing further the far-field divergence angle.

This work was supported by the National Science Fund for Distinguished Young Scholars of China (No. 60525406), the National Natural Science Foundation of China (Nos. 60736031, 60806018, and 60906026), the National Basic Research Program of China (No. 2006CB604903), and the National High Technology Research and Development Program of China (Nos. 2007AA03Z446 and 2009AA03Z403).

The authors would like to thank P. Liang, Y. Hu, and H. Sun for their help in the processing.

References

1. J. Faist, F. Capasso, D. L. Sivco, C. Sirtori, A. L. Hutchinson, and A. Y. Cho, Science **264,** 553 (1994).
2. A. Li, Chinese J. Lasers (in Chinese) **37,** 2213 (2010).
3. Y. Peng, X. Wei, W. Wang, and M. Li, Acta Opt. Sin. (in Chinese) **30,** 2624 (2010).
4. C. Yan, G. Lu, and L. Qin, Chin. Opt. Lett. **8,** 595 (2010).
5. D. Hofstetter, J. Faist, M. Beck, and U. Oesterle, Appl. Phys. Lett. **75,** 3769 (1999).
6. W. Schrenk, N. Finger, S. Gianordoli, L. Hvozdara, G. Strasser, and E. Gornik, Appl. Phys. Lett. **77,** 2086 (2000).
7. C. Pflugl, M. Austerer, W. Schrenk, S. Golka, G. Strasser, R. P. Green, L. R. Wilson, J. W. Cockburn, A. B. Krysa, and J. S. Roberts, Appl. Phys. Lett. **86,** 211102 (2005).
8. S. Schartner, M. Austerer, W. Schrenk, A. M. Andrews, P. Klang, and G. Strasser, Opt. Express **16,** 11920 (2008).
9. G. Maisons, M. Carras, M. Garcia, O. Parillaud, B. Simozrag, X. Marcadet, and A. D. Rossi, Appl. Phys. Lett. **94,** 151104 (2009).
10. E. Mujagic, L. K. Hoffmann, S. Schartner, M. Nobile, W. Schrenk, M. P. Semtsiv, M. Wienold, W. T. Masselink, and G. Strasser, Appl. Phys. Lett. **93,** 161101 (2008).
11. E. Mujagic, M. Nobile, H. Detz, W. Schrenk, J. Chen, C. Gmachl, and G. Strasser, Appl. Phys. Lett. **96,** 031111 (2010).
12. G. Xu, V. Moreau, Y. Chassagneux, A. Bousseksou, R. Colombelli, G. Patriarche, G. Beaudoin, and I. Sagnes, Appl. Phys. Lett. **94,** 221101 (2009).
13. Q. Lu, W. Zhang, L. Wang, F.-Q. Liu, and Z. Wang, Electron. Lett. **45,** 53 (2009).
14. W. Guo, Q. Lu, J. Liu, W. Zhang, Y. Jiang, L. Li, L. Wang, F. Liu, and Z. Wang, J. Semicond. **31,** 114014 (2010).
15. W.-H. Guo, J.-Q. Liu, Q.-Y. Lu, W. Zhang, L. Li, L.-J. Wang, F.-Q. Liu, and Z.-G. Wang, Chin. Phys. B **19,** 054208 (2010).